






Optimizing two-qubit gates for ultracold fermions in optical lattices

Jan A. P. Reuter ^{1,2,*} Juhi Singh ^{1,2} Tommaso Calarco ^{1,2,3} Felix Motzoi ^{1,2} and Robert Zeier ^{1,†}

¹*Forschungszentrum Jülich GmbH, Peter Grünberg Institute,
Quantum Control (PGI-8), 52425 Jülich, Germany*

²*Institute for Theoretical Physics, University of Cologne, Zùlpicher Straße 77, 50937 Cologne, Germany*

³*Dipartimento di Fisica e Astronomia, Università di Bologna, 40127 Bologna, Italy*

(Dated: December 4, 2025)

Ultracold neutral atoms in optical lattices are a promising platform for simulating the behavior of complex materials and implementing quantum gates. We optimize collision gates for fermionic ⁶Li atoms confined in a double-well potential, controlling the laser amplitude and keeping its relative phase constant. We obtain high-fidelity gates based on a one-dimensional confinement simulation. Our approach extends beyond earlier Fermi-Hubbard simulations by capturing a momentum dependence in the interaction energy. This leads to a higher interaction strength when atoms begin in separate subwells compared to the same subwell. This momentum dependence might limit the gate fidelity under realistic experimental conditions, but also enables tailored applications in quantum chemistry and quantum simulation by optimizing gates for each of these cases separately.

I. INTRODUCTION

Quantum computation with neutral atoms in optical lattices has seen rapid progress due to the ability to scale to large atom numbers and to perform high-fidelity local operations [1–4]. A key challenge, however, remains the realization of fast and high-fidelity two-qubit gates that are compatible with scalable architectures. One promising approach is the use of collisional gates, where entanglement is generated through interactions when atoms are brought into contact [5–8]. This method leverages the s-wave scattering [9, 10] interaction between ultracold atoms and is inherently robust to certain types of noise. The concept of using controlled collisions in optical lattices for quantum gates was first proposed by [11], where the interaction-induced phase shift from s-wave scattering was used to implement entangling gates between atoms in adjacent lattice sites. Subsequent experiments with bosonic atoms, such as ⁸⁷Rb in double-well potentials [12–17], have demonstrated coherent two-body dynamics and entanglement generation via controlled tunneling and collisions. Recent attention has turned to fermionic systems [18–24], especially using atoms as ⁶Li, due to their favorable collisional properties, large Feshbach resonance tunability, and small mass which enables faster tunneling. Fermions offer additional advantages for quantum information processing, such as spin-encoded qubits [25] and Pauli-blockade induced noise protection [26]. Theoretical works as well as experiments have demonstrated local control over spin and position states of fermionic atoms in optical tweezers and lattices [27–30].

With precise control of the system, efficient single- and two-qubit operations are achieved. Recent works primarily employ different types of controls to steer the dynamics of the system and perform gates. Using a relative

phase between the lasers, single-qubit operations, specifically π -pulses, have been performed with an approximate fidelity of 0.993 and a pulse duration of about 500 μ s [29]. The longer pulse duration and its shape have been chosen to suppress excitations of the atom. The residual error arises from various noise sources, such as phase and intensity noise. Adjusting the amplitude of the lasers to change the barrier height between the wells, a recent experiment [30] performed a two-qubit entangling operation with a fidelity of 0.9975 and a gate duration of 1.2 ms. The gate sequence is designed to balance gate speed while limiting doublon creation.

These quantum operations have been performed with great precision, the gate durations and fidelities can be further improved using optimal control techniques. In this work, we build on earlier work and tools as in [31, 32] to optimize fermionic two-qubit entangling gates in a double well based on a one-dimensional (1D) confinement simulation, while controlling the laser amplitude and keeping its relative phase constant. To this end, we develop an alternative numerical simulation technique (see Sec. III A 1) which goes beyond the Fermi-Hubbard simulation in [32]. This simulation method is reasonably fast and allows for adequate precision. We benchmark it against the methods in [31, 32] (see Sec. III A 2) using realistic parameters from the recent experimental work [29]. Our simulation method is then combined with an innovative gradient-based optimization (see Sec. III B).

Based on the developed simulation and optimization methods, we observe characteristic differences compared to earlier work. The 1D confinement simulation highlights a momentum dependence of the interaction energy (see Sec. IV B) which results in a higher interaction strength for atoms starting in different subwells compared to atoms starting in the same subwell. This is not directly observable in the Fermi-Hubbard model as it does not consider the momentum information. The 1D confinement simulation enables us to optimize the two cases separately (see Sec. IV C) which is relevant for important applications in quantum chemistry [33] (starting

* ja.reuter@fz-juelich.de

† r.zeier@fz-juelich.de

from the same subwell) and in the context of quantum simulation and quantum computing [29, 30, 32] (starting in separate subwells). Finally, our optimized gates are robust against an asymmetric lattice due to a relative phase in the laser control and an error in the interaction energy which occurs due to uncertainties in the effective interaction (as shown in Sec. V). Moreover, we analyze how the gates are affected by state-preparation errors resulting in three particles in a single double well.

The manuscript introduces its physical system description and its target gate in Sec. II. It continues in Sec. III with the developed simulation and optimization methods and the corresponding results are detailed in Sec. IV. The robustness of our gates is discussed in Sec. V before we conclude.

II. SYSTEM DESCRIPTION

We consider localized ultra-cold fermionic ^6Li atoms in a three-dimensional optical lattice with coordinates $\mathbf{r} = (x, y, z)$. The corresponding optical potential $V(\mathbf{r}, t) = V(x, t) + V(y) + V(z)$ can be split into its three spatial components. The y - and z -components $V(y) = -V_y \cos^2(k_y y)$ and $V(z) = -V_z \cos^2(k_z z)$ are created by single standing waves and are kept constant with time. The x -direction is time dependent and contains two different standing waves

$$V(x, t) = V_s(t) \cos^2(k_x x + \varphi) - V_l(t) \cos^2\left(\frac{k_x}{2} x\right). \quad (1)$$

Here, V_s and V_l are the short and long lattice potential energies and they represent two of our controls of the system. The wave vectors of the laser fields are given by $k_d = \sin(\beta_d/2) 2\pi/(532\text{ nm})$ for $d \in \{x, y, z\}$, where the angles $\beta_x = \beta_y = 26.7^\circ$ and $\beta_z = 10.16^\circ$ between the laser fields are shallow and they correspond to the angles in [29, 30, 34]. The relative phase φ between the long and short lattice will in this work be set to zero, except for Sec. III A 2. In Fig. 1 one can see the resulting lattice in x -direction produced by the overlapping laser fields.

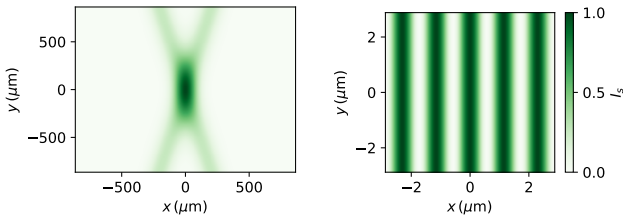


FIG. 1: **Optical lattice from a tilted laser field.** On the left, intensity of the laser field acting on the short lattice in the xy -plane with a characteristic angle of $\beta_x = 26.7^\circ$ between the two laser beams. On the right, a magnified version details the $\cos^2(k_x x)$ lattice.

Equation (1) has been simplified by neglecting the (approximate) Gaussian decay $\exp\{-2[x \cos(\beta_x/2)/w_s]^2\}$ of the laser intensity in the x -direction. We assume a laser with a Gaussian beam with beam waists of $w_s \approx 120\text{ }\mu\text{m}$ and $w_l \approx 220\text{ }\mu\text{m}$. Localized atoms in an optical lattice are considered to be in an maximally localized Wannier state $w(x)$. This state is an equal superposition of all Bloch states $e^{iqx}u_q(x)$ of that lattice $w(x) = \sum_q e^{i(qx+\chi_q)}u_q(x)/\sqrt{N}$ with a momentum depending phase χ_q and an arbitrary number N of sites in the lattice. We obtain the value of χ_q by solving the equation $xw(x-x_0) = x_0w(x-x_0)$, where x is the position operator in the Bloch basis and x_0 is the expectation value of the position. The double-well structure in the x -direction yields a symmetric (even) and an antisymmetric (odd) solution with a small band gap. The left (w_L) or right (w_R) localized Wannier states are then a superposition between the even $2n$ band and its subsequent odd $2n+1$ one [32, 35–37]. An example for the two lowest bands ($n = 0$) are shown in Fig. 2.

We now move from one to two atoms and aim at entangling two atoms with each other by applying a collision gate in the x -direction. The atoms sit both in one of the double wells created by $V(x, t)$. For the two-body Hamiltonian with coordinates $\mathbf{r}_j = (x_j, y_j, z_j)$, a pseudo potential is given by the δ -function which represents the s -wave scattering and results in

$$H(\mathbf{r}_1, \mathbf{r}_2, s_1, s_2, t) = \sum_{j=1}^2 -\frac{\hbar^2}{2m} \nabla_j^2 + V(\mathbf{r}_j, t) + U_{3D} \delta_{s_1, \bar{s}_2} \delta_{\text{reg}}(\mathbf{r}_1 - \mathbf{r}_2) \quad (2)$$

where $s_j \in \{\uparrow, \downarrow\}$ is the spin of the atom j with mass m (and $\bar{s}_j = \downarrow$ for $s_j = \uparrow$ and vice versa), $U_{3D} = 4\pi\hbar^2 a/m$ [9], a denotes the scattering length, and δ_{reg} is the regularized delta function [5, 7, 8].

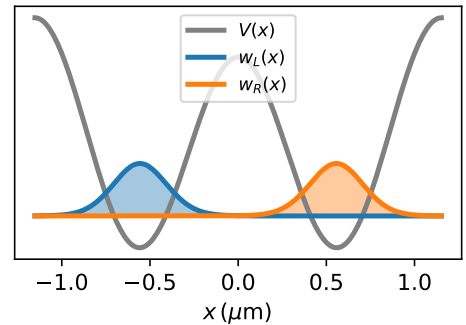


FIG. 2: **The maximally localized Wannier states.** The atoms are prepared in either the left or the right Wannier state. Both states are a superposition of the two lowest Bloch bands of the corresponding optical potential in the x -direction.

A. The s -wave scattering in the 1D confinement

As introduced above, the wave function of one atom has three geometric dimensions x , y , and z . Consequently, the wave function of two atoms is defined by the six-dimensional geometric space given by the coordinates $\mathbf{r}_j = (x_j, y_j, z_j)$. Or in general, the number of dimensions D of a combined wave function is the sum $D = \sum_j D_j$ of the dimensions D_j of the separated wave functions. Since the simulation time for such a problem grows exponential with the number of dimensions (see Sec. III A 1), we truncate the wave function. If one deals with a nearly harmonic potential, one can approximately neglect the “center of mass” part, e.g., $y_1 + y_2$, of the wave function based on its rotation symmetry as it is mostly decoupled from the distance part, e.g., $y_1 - y_2$. Alternatively, one can effectively describe each atom in lower confinements to truncate the wave function.

We consider the wave functions to be strongly confined in the y - and z -directions due to our assumption of a strong and narrow potential (similarly as in [31]). This allows us to neglect the dynamics in these directions during the collision, which is denoted as the 1D confinement since only one spatial degree of freedom remains. Thus confinement-induced resonances can occur with an effective 1D scattering potential $U_{1D}\delta(x_1 - x_2)$ [9, 38–40],

$$U_{1D} = -\frac{2\hbar^2}{ma_{1D}} \text{ and } a_{1D} = l_{\perp} \left(A - \frac{l_{\perp}}{a} \right),$$

where l_{\perp} is the oscillation length in the yz -plane and $A = 1.036$ has been numerically calculated [9, 41, 42].

B. Two-atom Wannier states in the 1D confinement

We have assumed until now that our atoms will be prepared in an initial state that is approximately a Wannier state of the optical lattice in Eq. (1) while neglecting any interaction between them. If, however, both atoms are localized on the same side of the double well, they will strongly interact with each other and the optical lattice alone can no longer define our initial state. Consequently, we need to define new two-atom Wannier states, which take also the interaction energy into account. The interaction potential is however not periodic and thus can not lead to Wannier states (as they need to be periodic, see the beginning of Sec. II). We can resolve this by using a Dirac comb $\sum_{n=-\infty}^{\infty} \delta[x_1 - x_2 - n2\pi/(\sqrt{2}k_x)]$ in addition to the optical lattice, instead of the single term corresponding to $n = 0$ in the sum. This results in a periodicity of $\sqrt{2}k_x$, which is big enough so that its effect on the Wannier state is approximately only given for $n = 0$.

In general, this holds for all four possible two-atom positions LL , LR , RL , RR . If both particles sit in different subwells, e.g., LR , their Wannier states can nearly perfectly described by the multiplication of the

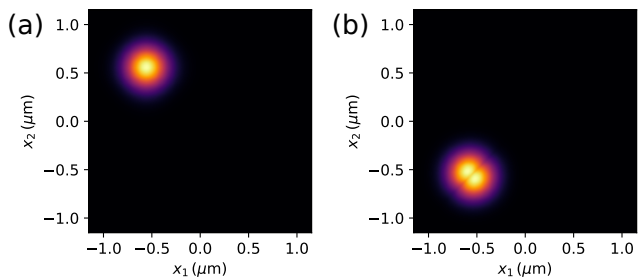


FIG. 3: **Wannier states of interacting atoms.** (a) shows the decoupled two-atom Wannier state with the first atom in the left state $w_L(x_1)$ and the second one in the right state $w_R(x_2)$. (b) shows the coupled two-atom Wannier state $w_{LL}(x_1, x_2)$, where the interaction energy at $x_1 = x_2$ divides the wave packet in two symmetric parts. We have recoil energies $V_s = 40E_{r,s}$, $V_l = 30E_{r,l}$, and a scattering length of $a_{1D} = -6675a_0$ with Bohr radius $a_0 \approx 52.9$ pm.

Wannier states of the separated atoms $w_{LR}(x_1, x_2) \approx w_L(x_1)w_R(x_2)$. In contrast to that, we need to calculate the new combined Wannier states for the cases where both particles sit in the same subwell [e.g., LL] by adapting to the interaction. These new Wannier states then represent already entangled particles since the wave packet is divided in two symmetric parts [see Fig. 3].

C. The quantum gate

We discuss the quantum gate that will be applied to the atoms. The potential energy of the laser field is chosen such that its values at the beginning and the end of the gate agree. Thus we can use the same Wannier basis to describe the initial and the target state and this Wannier basis represents our computational basis.

We start with the two associated Wannier states in the x -direction $|L\rangle := w_L(x)$, $|R\rangle := w_R(x)$ which are localized in the left or right subwell. We then define the operators $\hat{X} = |R\rangle\langle L| + |L\rangle\langle R|$ and $\hat{Z} = |L\rangle\langle L| - |R\rangle\langle R|$ and this allows us to describe the single-atom target gate as a partial rotation around $-\hat{X}$ by an angle α , i.e.,

$$\hat{P}_{T,1}(\alpha) = \exp \left[-i\frac{\alpha}{2}(-\hat{X}) \right]. \quad (3)$$

The minus sign in $-\hat{X}$ is arbitrary and originates from the fact that we choose $w_R(x) = w_L(-x)$. For two atoms, one first defines an operator $\hat{\delta} = (\hat{1} \otimes \hat{1} + \hat{Z} \otimes \hat{Z})/2$ representing the interaction in our computational basis, which is possible as we consider only interactions on a single side of the double well. Thus we consider

$$\hat{\mathcal{H}} = -\frac{\sqrt{3}}{4}(\hat{X} \otimes \hat{1} + \hat{1} \otimes \hat{X}) + \hat{\delta}$$

which resembles the two-band Hubbard-model Hamiltonian. To maximally entangle two atoms starting with

one atom sitting on the left $|L\rangle$ and the other one on the right $|R\rangle$, one chooses $U/J = 4/\sqrt{3}$ [15, 16] as in the Hubbard model. We can define a partial transition gate for two atoms as

$$\hat{P}_{T,2}(\alpha) = \exp(-i\alpha\hat{H}). \quad (4)$$

In each case, our gate takes only the position of the atoms into account and assumes fixed, opposite spins. To decompose the total quantum state into a position-spin basis, one has to respect the Pauli principle and needs to use the Slater determinant. Table I details a look-up table with all 16 possible cases in a double well for zero to four atoms in the lowest band.

We summarize the complete optimization procedure of Sec. IV in Fig. 4. This optimization procedure is tailored to minimize the total time of the optimization. We first optimize the time-dependent intensity of the short $V_s(t)$ and long $V_l(t)$ lattice for a single particle (which has by far the lowest computation time). Using the optimized $V_s(t)$ and $V_l(t)$ and keeping them unchanged, the gate is then optimized in the two-particle subspace (which has an intermediate computation time) based on the 1D-confinement approach by varying the time-constant effective scattering length a_{1D} . After these state-to-state optimizations, we simultaneously optimize $V_s(t)$, $V_l(t)$, and a_{1D} in the last step via a gate optimization (which is computationally the most expensive step) using the results from the first two preoptimizations as an initial guess. Finally, we will test the robustness of the gate optimization in Sec. V.

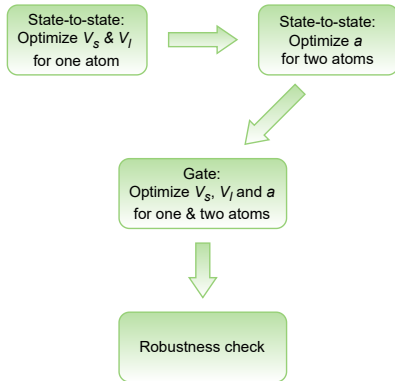


FIG. 4: **The optimization process as a flow chart.** In the first three steps, we optimize the laser intensities V_s , V_l and the effective scattering length a_{1D} . In the last step, we check of the robustness of the gate optimization (see Sec. V). This optimization procedure is tailored to minimize the total time of the optimization (see text).

III. SIMULATION AND OPTIMIZATION METHODS

A. Numerical time evolution

A common approach to solve the Schrödinger equation for a continuous wave function is to use a split-step method [31, 43], where we switch between the real and the momentum space. This method relies on a first order Trotterization of the time evolution operator and uses a fast Fourier transform (FFT) \mathcal{F} to diagonalize the kinetic energy part of the Hamiltonian [44–46]:

$$e^{-iH(x,t)\frac{dt}{\hbar}} \approx e^{-iV(x,t)\frac{dt}{2\hbar}} \mathcal{F}^\dagger e^{-i\frac{(\hbar q)^2}{2m}\frac{dt}{\hbar}} \mathcal{F} e^{-iV(x,t)\frac{dt}{2\hbar}}. \quad (5)$$

The FFT acts on the whole wave function to provide global information about the momentum, instead of using a discrete local approximation of the second derivative. Thus one only needs a few grid points in the real and momentum space for a good approximation of the time evolution. But the computation time of the parallelized FFT is still the largest part of the simulation time and is given by $\mathcal{O}(N \log(N))$, where N is the number of grid points. Since N grows in general exponentially with the number of spatial dimensions of the wave function, the computation time increases very unfavourably. We aim for a faster approach, as we will simulate many iterations of our two atom-gate, each with a different set of controls, to find the one which gives us the best result.

1. Alternative “leapfrog” method

We will now introduce an approach for which the computation time grows approximately linearly with N . We use a Numerov-type ansatz [47] which is applied to the time instead of a spacial dimension and where we approximate the total differential of the wave function in time with

$$\psi(t+\frac{dt}{2}) - \psi(t-\frac{dt}{2}) \approx -\frac{idt}{\hbar} H(t)\psi(t) \quad (6)$$

up to first order by inserting the Schrödinger equation for the time derivative. The resulting integration method evokes the leapfrog method [48] from classical mechanics.

For the second derivative in real space given by the Hamiltonian in Eq. (2), we choose a discrete third-order approximation with periodic boundary conditions. As we assume a periodic potential, one could also perform the simulation in momentum space, which would render the third-order approximation of the second derivative unnecessary. Nevertheless, we test the simulation method in real space and its applicability to general potentials where this speedup would not be applicable.

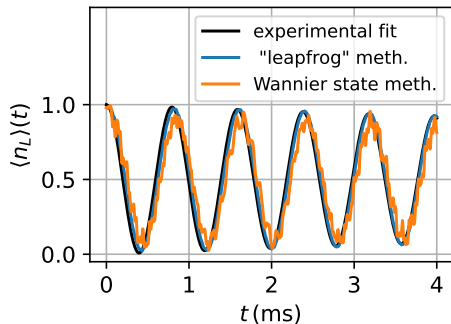


FIG. 5: **Benchmark 1.** Simulated Rabi oscillations of non-interacting atoms between the left and the right side of a double-well lattice. The blue line is calculated using Eq. (6) while the orange line uses the method from Ref. [32]. The black line corresponds the experimental data [29] which is almost superimposed with the blue line. The damping of the oscillation amplitude is caused by atoms hopping out of their initial well.

2. Benchmarking the simulation method

We test our simulation method from Sec. III A 1 and compare it with other methods from prior work [31, 32].

Benchmark 1. In the first test, we will repeat the procedure of [29] and compare our simulation results, obtained with the “leapfrog” method, to their experimental data in Fig. 5. We consider an ensemble of non-interacting atoms in a 1D superlattice, which is initially prepared in the lowest left-localized Wannier state of an asymmetric double well with non-zero relative phase φ . Then the relative phase is changed linearly within the first 0.05 ms between the long and the short lattice to initiate the Rabi oscillations between the left and the right well. To include the effect of atoms hopping to neighboring wells, a single atom is simulated starting in a central double well, which is surrounded by two other double wells. The total probability of finding an atom in the left subwell is obtained by integrating the squared absolute value of the wave function over the left half of each double well. We refer to [29] for a detailed description of the experimental procedure including all of the physical parameters. Additionally, we simulate the same setup with the simulation method of [32] to compare it to our “leapfrog” method. In [32], the quantum state and the Hamiltonian are described in a Wannier basis and one projects both of them into a new Wannier basis every time the potential changes; in other words, they use a Fermi-Hubbard simulation with higher bands. We validate that our method can capture the physics from the Fermi-Hubbard simulation in [32].

In Fig. 5, the simulation result of our “leapfrog”-method matches almost perfectly with the measured Rabi oscillations of [29] which was given by $\langle n_L \rangle(t) = [1 + \cos(\omega t) \exp(-t/\tau_d)]/2$ with $\omega = 2\pi \cdot 1.261(1)$ kHz

and $\tau_d = 27(3)$ ms. Also the simulation result using the “Wannier state”-method from [32] roughly agrees, even though the oscillation shows a jitter which results from the limited amount of basis states and it is only slowly reduced by enlarging the number of basis states. The simulation was performed with potentials energies of $V_s = 10.3E_{r,s}$ and $V_s = 31.9E_{r,l}$, which is in the range of the measured experimental laser intensities [29, 34] of $V_s = 10(0.5)E_{r,s}$ and $V_s = 31(1)E_{r,l}$. The computation time for the two simulations have been 0.19 s + 5.87 s with our method and 14.45 s + 1.44 s with the “Wannier state”-method from [32]. The first number marks the time which was needed to simulate the period where the relative phase has been changed, while the second one marks the time where the potential stays time independent. This is not unexpected, because [32] requires to calculate a new set of Wannier states at each time step in the first part, which is computationally expensive. Vice versa, it is cheaper to calculate the time evolution for a small time-independent Hamiltonian in the second part. In comparison, our method does only slightly depend on the change from a time-dependent potential to a stationary one.

Benchmark 2. We will now simulate two atoms that have been initially prepared in the ground state of two Gaussian traps. We will consider these traps to be harmonic, which is a good approximation for small deviations from the center of each trap. Consequently, we can write their corresponding ground state as $\psi_0(x) = \exp[-(x \pm d/2)^2/(2\sigma^2)]/\sqrt{\sqrt{\pi}\sigma}$ with a relative distance d between the traps. At time $t=0$, we will turn off the initial harmonic traps and turn on a shallower harmonic potential $V(x) = m\omega^2 x^2/2$ centered between the two atoms with a variance $\hbar/(2m\omega) \gg \sigma^2/2$, which is much bigger than the one from the initial traps. The considered physical parameters are $d = 2.329 \mu\text{m}$, $\sigma = 0.148 \mu\text{m}$, and $\omega = 2\pi \cdot 43.671$ MHz. The 1D interaction energy is given by the pseudo potential described in Sec. II A. This simulation setup was initially considered in [31], which aims

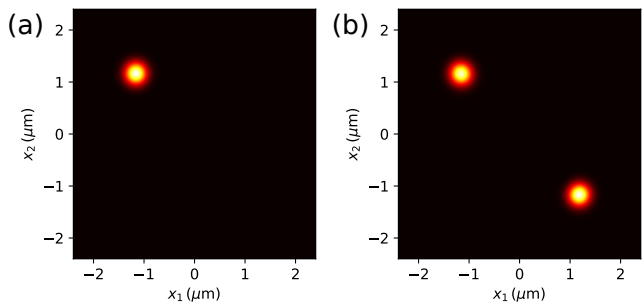


FIG. 6: **Benchmark 2.** An initial Gaussian wave packet ψ_0 is placed in a broad centered harmonic trap (left panel). Due to the interaction energy at $x_1 = x_2$, the wave packet splits up into two equal Gaussian wave packets with a relative phase of $-i$ (right panel).

at creating an entangling $\sqrt{\text{SWAP}}$ gate, but with fixed harmonic traps instead of a variable double-well potential. We apply the same physical and numerical parameters as in their work. This specific problem can now be solved in two ways, either with a 2D simulation or in two 1D simulations, since one can use the rotational symmetry of the Hamiltonian to separate the distance $x_1 - x_2$ from the center of mass $x_1 + x_2$. We will simulate both possibilities and compare their fidelity and computation time. The fidelity of our method is 0.9974 with a computation time of 505.64 s (2D) and 0.9975 within 6.29 s ($2 \times 1D$). The fidelity of the Fourier method is 0.9974 with a computation time of 537.73 s (2D) and 0.9976 within 19.11 s ($2 \times 1D$). As a comparison, [31] obtains a fidelity of 0.9979. In Figure 6, one can see the initial and final state of the simulation for our method in 2D, which is almost identical to the simulation in [31]. This can be seen as a validation of our simulation method as it yields reliable results for time-dependent potentials and for more than one simulated dimension.

B. Gradient-based optimization method

The combined gate infidelity $\epsilon = 1 - (|O_1|^2 + |O_2|^2)/2$ describes how well our optimized gates match with the corresponding target gates [Eqs. (3)-(4)], where

$$|O_1|(\alpha, \tau) = \text{Tr}(|\hat{P}_{T,1}^\dagger(\alpha)\hat{\Psi}_1(\tau)|)/2$$

is used for single atoms and

$$|O_2|(\alpha, \tau) = \text{Tr}(|\hat{P}_{T,2}^\dagger(\alpha)\hat{\Psi}_2(\tau)|)/4$$

for two atoms. Here, τ is the gate time and the matrices $\hat{\Psi}_i$ are defined below. In the definition of the unitary gate infidelity ϵ , we chose the equal weight of 1/2 between the single- and the two-atom gate since we will apply our pulses globally to all atoms in an optical lattice. While some of them are sitting in pairs in one of the double wells, others may remain isolated in a single subwell during the gate. The decision which and how many atoms will be paired or isolated, depends on the specific algorithm. Consequently we need to ensure that one suitable gate is applied for both paired and isolated atoms. To obtain the matrices $\hat{\Psi}_1(\tau)$ and $\hat{\Psi}_2(\tau)$, we apply the simulation for each state $\psi_n \in \{w_L, w_R\}$ or $\psi_n \in \{w_{LL}, w_{LR}, w_{RL}, w_{RR}\}$ and then calculate $\hat{\Psi}_{n,m}(\tau) = \int_{-\infty}^{\infty} \psi_m^*(x)\psi_n(x, \tau)dx$. We then determine the gradient $\partial_c \epsilon = -(|O_1|\partial_c|O_1| + |O_2|\partial_c|O_2|)$ of the infidelity with respect to a given control c (such as the scattering length). The gradient of the state $\psi'_{c,n} := \partial_c \psi_n$ can then be simulated by taking the derivative of the Schrödinger equation in [49, 50] and by solving

$$i\hbar \partial_t \psi'_{c,n}(x, t) = H(x, t)\psi'_{c,n}(x, t) + H'_c(x, t)\psi_n(x, t).$$

A similar equation can then be defined for the Hessian or higher derivatives of the state if needed. If $\psi'_{c,n}$ is zero

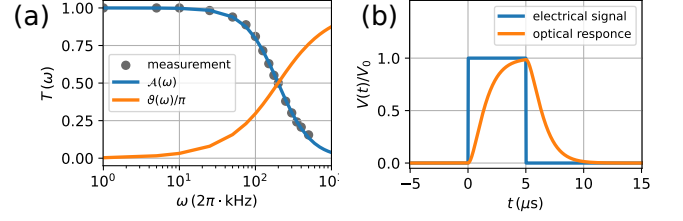


FIG. 7: **Transfer function for the electrical signal and its resulting optical response.** The Butterworth transfer function in (a) [34] yields the piece-wise constant electrical signal block in (b) which has a delayed optical response.

at $t = 0$, we only need to simulate the state gradient during the time where H'_c is non-zero. Afterwards the equation is just a normal Schrödinger equation and we can use back propagation to calculate the gradient of the infidelity. The only control for which the gradient is not zero at $t = 0$ is the scattering length since the Wannier states at the same subwell (see Fig. 3) depend on the interaction energy. In general, to calculate the gradient of a Wannier state w'_c , we determine the derivative of the defining equation $\partial_c [(x - x_0)w(x - x_0)] = 0$ (see the beginning of Sec. II) and also the derivative of the stationary Schrödinger equation $\partial_c [(H(x) - E)e^{iqx}u_q(x)] = 0$ as x is given in the Bloch basis.

C. Transfer function

The optical potential will be created in an experiment via a piece-wise constant signal with a step size of $\Delta t = 5 \mu\text{s}$ [34] from an electrical signal $V_{\text{el}}(t)$ which is sent to an optical device. In an experiment with a finite bandwidth, the optical response would no longer be piece-wise constant. The optical signal is calculated using the Fourier transform $\tilde{V}_{\text{el}}(\omega)$ of the electrical signal $V_{\text{el}}(t)$ (see, e.g., page 85 of [51]), i.e.,

$$V_{\text{el}}(t) = \sum_{n=1}^{\tau/\Delta t} V_n \text{rect}\left[t - \left(n - \frac{1}{2}\right)\Delta t\right],$$

$$\tilde{V}_{\text{el}}(\omega) = \frac{\Delta t}{\sqrt{2\pi}} \text{sinc}\left(\frac{\omega\Delta t}{2}\right) \sum_{n=1}^{\tau/\Delta t} V_n e^{i(n - \frac{1}{2})\omega\Delta t}.$$

Then one multiplies the Fourier transform of the electrical signal with the complex Butterworth transfer function $T(\omega) = \mathcal{A}(\omega)e^{i\vartheta(\omega)}$ from the optical part of the system. The transfer function consists of an amplitude damping $\mathcal{A}(\omega)$ as well as a phase shift $\vartheta(\omega)$ for higher frequencies as detailed in Fig. 7(a). We then transform it back to get the optical response

$$V_{\text{opt}}(t) = \frac{1}{\sqrt{2\pi}} \int_{-\infty}^{\infty} T(\omega) \tilde{V}_{\text{el}}(\omega) e^{-i\omega t} d\omega.$$

To characterize the frequency response of the optical system, the experimentalists [34] applied a sequence of programmed piece-wise constant drive signals to an acousto-optic modulator (AOM) and recorded the resulting optical intensity using a high-bandwidth photodetector. By varying the step duration Δt (corresponding to drive frequencies $f = 1/\Delta t$), the relative amplitude and phase response of the system were extracted and used to determine the complex transfer function $T(\omega)$. The resulting amplitude attenuation and phase delay are shown in Fig. 7(a), and this measured transfer function is employed in the reconstruction of the optical waveform $V_{\text{opt}}(t)$. This straight-forward approach nicely works in our case to determine the transfer function. If nonlinear effects in the transfer function become relevant, further approaches are available to determine the transfer function and to apply it in the optimization [52–54].

The number of piece-wise constant control values V_n in our optimization is given by $\tau/\Delta t$, while the system itself will only see the optical response obtained by applying the transfer function. For the gradient-based optimization, one would only need to simulate the gradient with respect to V_n from $t = (n-1)\Delta t$ until $t = n\Delta t$ if one has an actual piece-wise constant optical response from the optical device. In our case, we need to simulate the gradient until the optical response is zero again, which is approximately at $t = (n+2)\Delta t$ as one can see in Fig. 7(b).

IV. OPTIMIZING $V_s(t)$, $V_l(t)$ AND a_{1D} USING A 1D-CONFINEMENT SIMULATION

Before we optimize our three controls given by $V_s(t)$, $V_l(t)$, and the effective scattering length a_{1D} for a gate optimization, we first focus in Sec. IV A on the single-atom case and optimize only the intensity of the short and the long lattice for different transition ratios α between left and right. We then take the optimized pulse and apply it to a simulation of two atoms while only optimizing the scattering length for each of those pulses. In the second step (see Sec. IV B), we optimize all three controls again, but this time simultaneously in a gate optimization where the previous results are taken as an initial guess. This is motivated by the fact that the simulation time for two atoms grows quadratically due to a quadratic growth in the composite Hilbert space, while the simulation time for a single atom only grows linearly. Additionally, the optimization algorithm needs more iterations to find a solution for the time-dependent pulses $V_s(t)$ and $V_l(t)$ as well as for the time-constant parameter a_{1D} . Therefore, one wants to simulate only a few iterations with two atoms, especially for $V_s(t)$ and $V_l(t)$.

A. State-to-state preoptimization

We will now apply the gradient-based optimization algorithm BFGS [55], used previously in the context

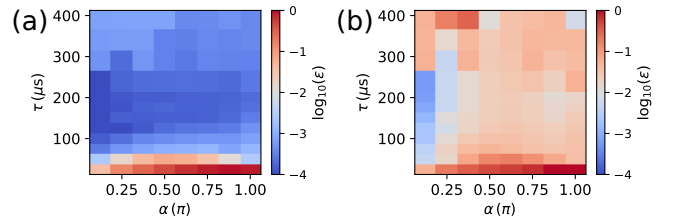


FIG. 8: **Infidelity of the state-to-state preoptimization.** Following our flow chart in Fig. 4 (see Sec. II C), we show the results of the first two steps corresponding to the state-to-state optimizations in both subfigures: (a) The logarithm of the infidelity for a single-atom optimization of the lattice intensities $V_s(t)$ and $V_l(t)$. (b) Same for the two-atom optimization of the effective scattering length a_{1D} , where the time-dependent parameters are left unchanged. The infidelity for the single-atom swap is much smaller than for an entangling collision of two atoms.

of the quantum optimal control method GRAPE [56] for quasi-Newton [53, 57] and Newton [58] optimizations. Thus, we find the best pulse for different gate times $\tau \in [25 \mu\text{s}, 400 \mu\text{s}]$ and different transition ratios $\alpha \in [\pi/8, \pi]$ when starting with an atom in the left (L) Wannier state and moving to the right (R) Wannier state. Since we are not breaking the symmetry of the potential during the state-to-state optimization, we do not need to include the reversed transition (from R to L). The Wannier state corresponds to an optical lattice with respective recoil energies of $V_s(0) = 40E_{r,s}$ and $V_l(0) = 30E_{r,l}$. Using the target gate $\hat{P}_{T,1}(\alpha)$ from Eq. (3), we can define a target state as $|\psi_{T,1}(\alpha)\rangle = \hat{P}_{T,1}(\alpha)|w_L\rangle$. In general, we define the infidelity for a state-to-state optimization by

$$\epsilon = 1 - |\langle\psi_T(\alpha)|\psi(\tau)\rangle|^2,$$

where $|\psi_T(\alpha)\rangle$ describes a general target state. We use this definition in this subsection and in Fig. 10 in Sec. IV C. In Fig. 8(a), we can see that we get quite good results for a single-atom transition with gate times above $\tau > 50 \mu\text{s}$. For shorter gate times, we are only limited by technical restrictions such as the piece-wise constant steps size Δt or the maximal recoil energies of the laser system. For two atoms as detailed in Fig. 8(b), we obtain higher infidelities for the target state $|\psi_{T,2}(\alpha)\rangle = \hat{P}_{T,2}(\alpha)|w_{L,R}\rangle$ [see Eq. (4)] as the optimization of $V_s(t)$ and $V_l(t)$ does not consider the interaction, as explained in Sec. II C. Nevertheless, this result is a good starting point for the gate optimization with one and two atoms.

B. Unitary gate optimization

The preoptimized controls for $V_s(t)$, $V_l(t)$, and the effective scattering length a_{1D} are now used as initial guesses for our gate optimization and this yields the pulse

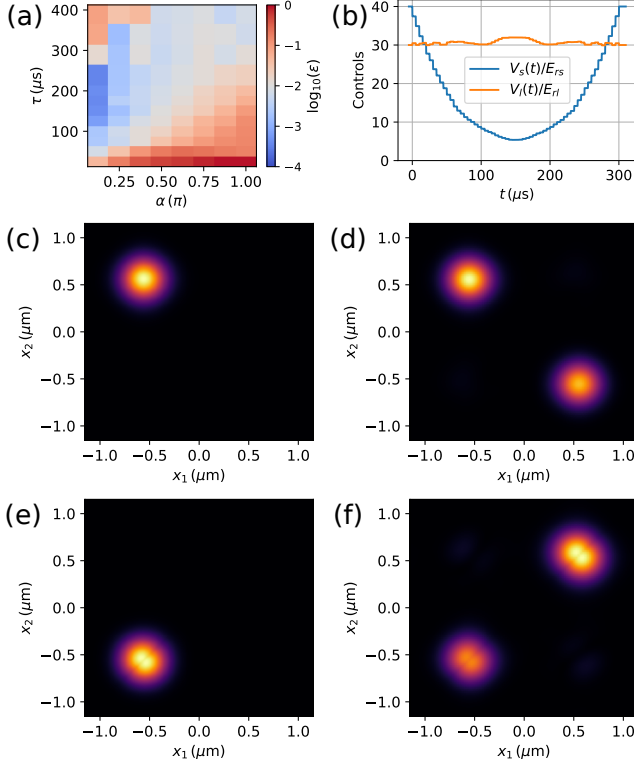


FIG. 9: **Optimization results.** Following our flow chart in Fig. 4 (see Sec. II C), we show the result of the third step corresponding to the gate optimization in subfigure (a). (a) Logarithm of the infidelity from the gate optimization of the lattice intensities $V_s(t)$, $V_l(t)$ and the effective scattering length a_{1D} . (b) Optimized pulse for $\alpha = \pi$, $\tau = 300 \mu\text{s}$ with an optimal scattering length of $a_{1D} = -11925a_0$. (c) and (e) Absolute value of the two basis states w_{LR} and w_{LL} [where (c) agrees with Fig. 3(a)]. (d) and (f) The final states after applying the pulse from (b) to the initial states in (c) and (e).

. The infidelities ϵ are 0.79% for (d) and 3.75% for (f).

shape and the associated dynamics shown in Fig. 9. The logarithm of the error plotted in Fig. 9(a) reveals a linear dependency of the gate time τ on the transition ratio α . The minimal ratio $\tau/\alpha \approx 300/\pi \mu\text{s}$ results in an error of approximately 1%. Figure 9(b) shows an example of a pulse with $\alpha = \pi$, $\tau = 300 \mu\text{s}$, while Figs. 9(d) and 9(f) illustrate the respective simulation results at final time, where the goal for $\alpha = \pi$ was to end in an equal superposition between w_{LR} and w_{RL} in Fig. 9(d) or between w_{LL} and w_{RR} in Fig. 9(f). While the optimization managed to reduce the mixture between the two cases in 9(d) and 9(f), we have not obtained a perfectly equal superposition. On the other hand, the scattering length of $a_{1D} = -11925a_0$ with a Bohr radius of $a_0 \approx 52.9 \text{ pm}$ is too high if the atoms start in different subwells in Fig. 9(c) and too low if they start in the same subwell in Fig. 9(e). As discussed before, the most limiting factor is the piece-wise constant step size $\Delta t = 5 \mu\text{s}$. It would

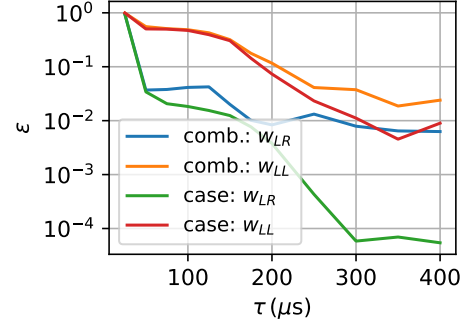


FIG. 10: **Infidelity of the combined optimization vs. the case optimization.** One can see a clear advantage for what we denote as a case optimization by performing a separate optimization for different initial states as compared to a combined optimization for all initial states at the same time. Especially for two atoms starting at different sides of the double well (w_{LR}), we gain two orders of magnitude in precision for longer gate times.

be advantageous to reduce it at least by a factor of 2 and increase the maximal recoil energy $E_{r,l}$ of the attractive long lattice by a factor of approximately 1.5. Then one would have a lot more freedom for short pulses and one could probably lower the minimal ratio of τ/α .

C. Case optimization for different initial states

In Sec. IV B, we optimized pulses to obtain the unitary gates $\hat{P}_{T,1}$ and $\hat{P}_{T,2}$ for the one- and the two-particle basis, respectively. This has resulted in an error of approximately 1% under experimentally realistic assumptions. Nevertheless, we now aim at separating the optimization of the two two-atom cases, where we start from the same subwell (w_{LL} or w_{RR}) or different subwells (w_{LR} or w_{RL}) as detailed in Sec. IV A. This separation is motivated by the fact that some applications considers only one of these two cases, while the other one is neglected. While the applications for starting in different subwells is discussed in the context of quantum simulation and quantum computing [29, 30, 32], the case of starting in the same subwell has applications in quantum chemistry [33]. Furthermore, the stand-alone optimization for the separate cases should yield much better results than the combined optimization in Sec. IV B. This approach is mainly focused on the transition ratio $\alpha = \pi$ as its final state is an equal superposition of the two possible states of the same case it started with. Numerically, the separation here means that we perform two optimizations, while calculating only the columns of $\hat{\Psi}_{n,m}(\tau)$ from Sec. III B by starting in one of the two cases and setting the columns for starting from the respective other case to zero.

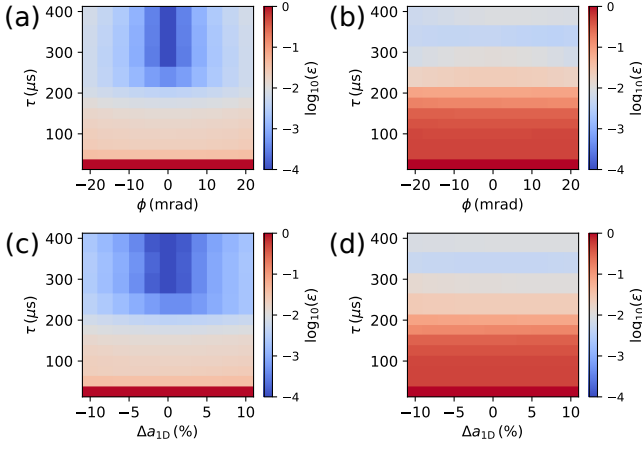


FIG. 11: **Robustness check.** Two atoms starting on different sides of the double well (w_{LR}) in (a) and (c) are more sensitive to slight changes of the relative phase ϕ and the effective scattering length a_{1D} compared to two atoms starting on the same side (w_{LL}) in (b) and (d).

Even when we optimize the two two-atom cases separately, we still include the one-atom case in both optimizations, as our pulses need to be also applicable to single atoms in a double well. For $\alpha = \pi$, Figure 10 compares the results of the combined optimization from Sec. IV B with the case optimization from this section. In both cases, the case optimization results in a significant decrease in the infidelity. If the atoms start on different sides of the double well, the difference is around two orders of magnitude for gate times $\tau \geq 300 \mu\text{s}$. One also sees an advantage by separating the optimization if the atoms start in the same subwell, even though the difference in this case is smaller. Why do the results of the two cases appear to be quite different? The reason is that two atoms starting on the same side (w_{LL} or w_{RR}) will also move into the same direction. Or in other words, they will have similar momenta q_j . The problem is that the interaction potential only affects the parts of the wave function which have opposite momenta, which is particularly relevant for the case of the atoms starting in opposite subwells (w_{LR} or w_{RL}). One can check this by taking the Fourier transformation of the pseudo-potential $\mathcal{F}[\delta(x_1 - x_2)] = \delta(q_1 + q_2)$.

V. ROBUSTNESS AGAINST SYSTEM IMPURITIES

For the optimizations in the previous sections, we have assumed perfect conditions which will not be given in realistic experiments. We now analyze possible deviations from that perfect scenario and consider their effect on the behavior of the atoms.

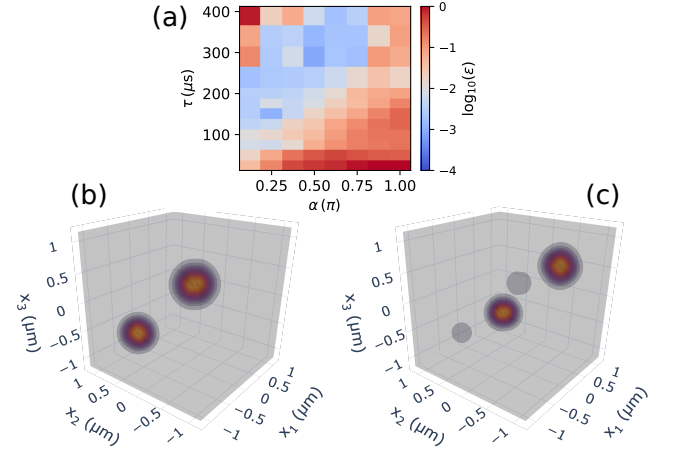


FIG. 12: **Three-atom collision.** (a) The logarithm of the infidelity of the three-atom collision in the 1D confinement. (b) The starting state $(w_{LLR} - w_{LRL})/\sqrt{2}$ and (c) the final state for $\tau = 250 \mu\text{s}$ and $\alpha = \pi$ after simulating the system with the pulse from Fig. 9. The final state also observes higher excitations beyond the ground states as well as a population remaining in the initial state.

A. Asymmetric lattice and interaction uncertainty

During the whole optimization process, we have assumed a perfectly symmetric lattice which corresponds to a relative phase of $\varphi=0$ in Eq. (1). Furthermore, we have considered a direct and simple mapping from the applied magnetic field to the effective one-dimensional scattering length a_{1D} . Both assumptions need to be considered carefully and we analyze the effects of the uncertainty on our optimized pulses. We will now test our optimized pulses from Sec. IV C for different values of a time-constant non-zero relative phase and for deviations from the optimal scattering length. In Fig. 11, we can see the infidelity of the case-optimized pulses from Sec. IV C for the two cases of both atoms starting on different sides, in Figs. 11(a) and 11(c), or on the same side of the double well, in Figs. 11(b) and 11(d). One observes that the two atoms starting on different subwells and colliding into each other are more sensitive to errors than the two atoms starting on the same subwell. But one has to remark that we have used in Fig. 11(b) a slightly different target state $(w_{LL} + \exp[i\gamma(\tau)] \cdot w_{RR})/\sqrt{2}$ with a time-dependent phase γ as we now explain. Due to the relative phase of the lattice, the left and the right side of the double well do not have the same potential energy. Consequently, the atoms gain a time-dependent phase γ during the operations of the gate that is roughly proportional to twice the energy difference between the states on the left and the right side of the double well. Nevertheless, both cases appear to be quite robust against deviations from the perfect scenario, which is promising for an experimental realization.

TABLE I: **Mapping from the total quantum state to the position-spin basis.** The total quantum state is decomposed into the position-spin basis with the help of the Slater determinant. We consider all 16 possible cases in a double well with zero to four atoms in the lowest band.

total quantum state	position-spin state
$ 00\rangle$	$ \text{vacuum}\rangle$
$ \uparrow 0\rangle$	$ L\rangle_1 \otimes \uparrow\rangle_1$
$ 0\uparrow\rangle$	$ R\rangle_1 \otimes \uparrow\rangle_1$
$ \downarrow 0\rangle$	$ L\rangle_1 \otimes \downarrow\rangle_1$
$ 0\downarrow\rangle$	$ R\rangle_1 \otimes \downarrow\rangle_1$
$ \uparrow\downarrow\rangle$	$(L\rangle_1 R\rangle_2 \otimes \uparrow\rangle_1 \downarrow\rangle_2 - R\rangle_1 L\rangle_2 \otimes \downarrow\rangle_1 \uparrow\rangle_2)/\sqrt{2}$
$ \downarrow\uparrow\rangle$	$(R\rangle_1 L\rangle_2 \otimes \uparrow\rangle_1 \downarrow\rangle_2 - L\rangle_1 R\rangle_2 \otimes \downarrow\rangle_1 \uparrow\rangle_2)/\sqrt{2}$
$ D0\rangle$	$ L\rangle_1 L\rangle_2 \otimes (\uparrow\rangle_1 \downarrow\rangle_2 - \downarrow\rangle_1 \uparrow\rangle_2)/\sqrt{2}$
$ 0D\rangle$	$ R\rangle_1 R\rangle_2 \otimes (\uparrow\rangle_1 \downarrow\rangle_2 - \downarrow\rangle_1 \uparrow\rangle_2)/\sqrt{2}$
$ \uparrow\uparrow\rangle$	$(L\rangle_1 R\rangle_2 - R\rangle_1 L\rangle_2) \otimes \uparrow\rangle_1 \uparrow\rangle_2/\sqrt{2}$
$ \downarrow\downarrow\rangle$	$(L\rangle_1 R\rangle_2 - R\rangle_1 L\rangle_2) \otimes \downarrow\rangle_1 \downarrow\rangle_2/\sqrt{2}$
$ D\uparrow\rangle$	$(L\rangle_1 R\rangle_2 - R\rangle_1 L\rangle_2) L\rangle_3 \otimes \uparrow\rangle_1 \uparrow\rangle_2 \downarrow\rangle_3/\sqrt{6}$ $- (L\rangle_1 R\rangle_3 - R\rangle_1 L\rangle_3) L\rangle_2 \otimes \uparrow\rangle_1 \downarrow\rangle_2 \uparrow\rangle_3/\sqrt{6}$ $+ (L\rangle_2 R\rangle_3 - R\rangle_2 L\rangle_3) L\rangle_1 \otimes \downarrow\rangle_1 \uparrow\rangle_2 \uparrow\rangle_3/\sqrt{6}$
$ \uparrow D\rangle$	$(L\rangle_1 R\rangle_2 - R\rangle_1 L\rangle_2) R\rangle_3 \otimes \uparrow\rangle_1 \uparrow\rangle_2 \downarrow\rangle_3/\sqrt{6}$ $- (L\rangle_1 R\rangle_3 - R\rangle_1 L\rangle_3) R\rangle_2 \otimes \uparrow\rangle_1 \downarrow\rangle_2 \uparrow\rangle_3/\sqrt{6}$ $+ (L\rangle_2 R\rangle_3 - R\rangle_2 L\rangle_3) R\rangle_1 \otimes \downarrow\rangle_1 \uparrow\rangle_2 \uparrow\rangle_3/\sqrt{6}$
$ D\downarrow\rangle$	$ L\rangle_1(L\rangle_2 R\rangle_3 - R\rangle_2 L\rangle_3) \otimes \uparrow\rangle_1 \downarrow\rangle_2 \downarrow\rangle_3/\sqrt{6}$ $- L\rangle_2(L\rangle_1 R\rangle_3 - R\rangle_1 L\rangle_3) \otimes \downarrow\rangle_1 \uparrow\rangle_2 \downarrow\rangle_3/\sqrt{6}$ $+ L\rangle_3(L\rangle_1 R\rangle_2 - R\rangle_1 L\rangle_2) \otimes \downarrow\rangle_1 \downarrow\rangle_2 \uparrow\rangle_3/\sqrt{6}$
$ \downarrow D\rangle$	$ R\rangle_1(L\rangle_2 R\rangle_3 - R\rangle_2 L\rangle_3) \otimes \uparrow\rangle_1 \downarrow\rangle_2 \downarrow\rangle_3/\sqrt{6}$ $- R\rangle_2(L\rangle_1 R\rangle_3 - R\rangle_1 L\rangle_3) \otimes \downarrow\rangle_1 \uparrow\rangle_2 \downarrow\rangle_3/\sqrt{6}$ $+ R\rangle_3(L\rangle_1 R\rangle_2 - R\rangle_1 L\rangle_2) \otimes \downarrow\rangle_1 \downarrow\rangle_2 \uparrow\rangle_3/\sqrt{6}$
$ DD\rangle$	$(L\rangle_1 R\rangle_2 - R\rangle_1 L\rangle_2)(L\rangle_3 R\rangle_4 - R\rangle_3 L\rangle_4) \otimes (\uparrow\rangle_1 \uparrow\rangle_2 \downarrow\rangle_3 \downarrow\rangle_4 + \downarrow\rangle_1 \downarrow\rangle_2 \uparrow\rangle_3 \uparrow\rangle_4)/\sqrt{24}$ $- (L\rangle_1 R\rangle_3 - R\rangle_1 L\rangle_3)(L\rangle_2 R\rangle_4 - R\rangle_2 L\rangle_4) \otimes (\uparrow\rangle_1 \downarrow\rangle_2 \uparrow\rangle_3 \downarrow\rangle_4 + \downarrow\rangle_1 \uparrow\rangle_2 \downarrow\rangle_3 \uparrow\rangle_4)/\sqrt{24}$ $+ (L\rangle_1 R\rangle_4 - R\rangle_1 L\rangle_4)(L\rangle_2 R\rangle_3 - R\rangle_2 L\rangle_3) \otimes (\uparrow\rangle_1 \downarrow\rangle_2 \downarrow\rangle_3 \uparrow\rangle_4 + \downarrow\rangle_1 \uparrow\rangle_2 \uparrow\rangle_3 \downarrow\rangle_4)/\sqrt{24}$

B. Three-body collisions in the 1D confinement

Continuing the discussion on robustness, another possible error can occur during the state preparation which then yields three particles in a single double well, where the position state is $(w_{LLR} - w_{LRL})/\sqrt{2}$. Moreover, considering three spins with $s_2 = s_3 = \bar{s}_1$ (where $\bar{s}_j = \downarrow$ for $s_j = \uparrow$ and vice versa), we can then represent the spin states $|D\uparrow\rangle$ and $|D\downarrow\rangle$, and by spatial symmetry also $|\uparrow D\rangle$ and $|\downarrow D\rangle$, in the position basis. The three particle Hamiltonian is similar to

$$H(\{x_j, s_j\}, t) = \sum_{j=1}^3 -\frac{\hbar^2}{2m} \partial_{x_j}^2 + V(x_j, t) + U_{1D}[\delta(x_1 - x_2) + \delta(x_1 - x_3)].$$

According to the Hubbard model, the target gate for three particles is then given by $\hat{P}_{T,1}(\alpha) \otimes \hat{1} \otimes \hat{1}$.

In Fig. 12, the three-atom collision does not completely behave as expected, as we will explain now. Even when most of the population moves for $\alpha = \pi$ from $(w_{LLR} - w_{LRL})/\sqrt{2}$ to $(w_{RRL} - w_{RLR})/\sqrt{2}$, a non-negligible part results in higher excitations for gate times under 200 μs , or remains in the initial state for gate times over 300 μs . This is consistent as we have not optimized

for these error states. But the three-atom collision is not part of our focus and it is more important to know the result after the collision than to optimize for it. In principle, one could also simulate the case of four atoms $|DD\rangle$, but that system is more or less frozen due to the symmetry of the position state or in other words it is an eigenstate of the Fermi-Hubbard model and the result would be trivial, see Table I. Only for shorter pulses with higher kinetic energies and strong interactions, one would get higher excitations [32].

VI. CONCLUSION

We used precise simulation and optimization methods for two-qubit gates in ultra cold fermionic atoms using a 1D confinement and going beyond Fermi-Hubbard simulations. The simulation time approximately grows only linearly in the system size and results in a similar precision as for earlier approaches. Our optimizations provide a short entangling collision gate that can be applied in the experimental setting of [29]. We account for experimental upper bounds for the recoil energies in the laser system, a smallest possible time step for the piece-wise constant laser intensities, as well as a transfer function

from the electric signal to the optical response. This provides realistic predictions for experimental implementations. We have analyzed the robustness of our pulses with regard to an asymmetric lattice due to a relative phase of the laser field, an error in the interaction energy which occurs due to uncertainties in the effective interaction, and state preparation errors resulting in three atoms in the same double well, where the last case can be roughly approximated in the Fermi-Hubbard model.

Our results show a characteristic behavior of the interacting atoms depending on whether the initial state starts on the same or opposite sides of the double well. This presents an opportunity for optimizing the different initial states separately providing tailored optimizations for applications in quantum chemistry [33] and quantum simulation and quantum computing [29, 30, 32]. Further improvements to control sequences for two-qubit gates can be realized in the future with additional numerical and feedback-based optimizations while adapting to specific experimental constraints. This prepares the ground for efficient and robust gates in quantum computers and simulators with fermionic atoms.

ACKNOWLEDGMENTS

We thank Petar Bojović for measuring the transfer function [34], answering many questions, and providing feedback on the manuscript. We also thank Robin Groth, Titus Franz, Philipp Preiss, and Timon Hilker for insightful discussions about the fermionic system as well as for providing detailed experimental parameters. Jan Reuter would like to thank Erik Weerda, Niklas Tausendpfund, Daniel Alcalde and Matteo Rizzi for support during the initial stage of research and coding. Last but not least, we thank Eloisa Cuestas for additional comments and a last check up. We acknowledge support from the German Federal Ministry of Research, Technology and Space through the funding program quantum technologies—from basic research to market under the project FermiQP, 13N15891. We acknowledge funding under Horizon Europe programme HORIZON-CL4-2022-QUANTUM-02-SGA via the project 101113690 (PASQuanS2.1). JS has also been supported by the German Ministry of Research, Technology and Space through the funding program quantum technologies—from basic research to market under the project MUNIQC-Atoms, 13N16073.

-
- [1] D. Bluvstein, S. J. Evered, A. A. Geim, S. H. Li, H. Zhou, T. Manovitz, S. Ebadi, M. Cain, M. Kalinowski, D. Hangleiter, J. P. B. Ataides, N. Maskara, I. Cong, X. Gao, P. S. Rodriguez, T. Karolyshyn, G. Semeghini, M. J. Gullans, M. Greiner, V. Vuletić, and M. D. Lukin, Logical quantum processor based on reconfigurable atom arrays, *Nature* **626**, 58 (2024).
 - [2] S. J. Evered, D. Bluvstein, M. Kalinowski, S. Ebadi, T. Manovitz, H. Zhou, S. H. Li, A. A. Geim, T. T. Wang, N. Maskara, H. Levine, G. Semeghini, M. Greiner, V. Vuletić, and M. D. Lukin, High-fidelity parallel entangling gates on a neutral-atom quantum computer, *Nature* **622**, 268 (2023).
 - [3] F. Gyger, M. Ammenwerth, R. Tao, H. Timme, S. Snigirev, I. Bloch, and J. Zeiher, Continuous operation of large-scale atom arrays in optical lattices, *Phys. Rev. Res.* **6**, 033104 (2024).
 - [4] A. L. Shaw, Z. Chen, J. Choi, D. K. Mark, P. Scholl, R. Finkelstein, A. Elben, S. Choi, and M. Endres, Benchmarking highly entangled states on a 60-atom analogue quantum simulator, *Nature* **628**, 71 (2024).
 - [5] T. Busch, B.-G. Englert, K. Rzażewski, and M. Wilkens, Two cold atoms in a harmonic trap, *Found. Phys.* **28**, 549 (1998).
 - [6] T. Calarco, E. A. Hinds, D. Jaksch, J. Schmiedmayer, J. I. Cirac, and P. Zoller, Quantum gates with neutral atoms: Controlling collisional interactions in time-dependent traps, *Phys. Rev. A* **61**, 022304 (2000).
 - [7] Z. Idziaszek and T. Calarco, Two atoms in an anisotropic harmonic trap, *Phys. Rev. A* **71**, 050701 (2005).
 - [8] J.-J. Liang and C. Zhang, Two ultracold atoms in a completely anisotropic trap, *Phys. Scr.* **77**, 025302 (2008).
 - [9] I. Bloch, J. Dalibard, and W. Zwerger, Many-body physics with ultracold gases, *Rev. Mod. Phys.* **80**, 885 (2008).
 - [10] J. Sakurai and J. Napolitano, *Modern Quantum Mechanics*, 3rd ed. (Cambridge University Press, Cambridge, 2020).
 - [11] D. Jaksch, H.-J. Briegel, J. I. Cirac, C. W. Gardiner, and P. Zoller, Entanglement of atoms via cold controlled collisions, *Phys. Rev. Lett.* **82**, 1975 (1999).
 - [12] O. Mandel, M. Greiner, A. Widera, T. Rom, T. W. Hänsch, and I. Bloch, Controlled collisions for multi-particle entanglement of optically trapped atoms, *Nature* **425**, 937 (2003).
 - [13] T. Calarco, U. Dorner, P. S. Julienne, C. J. Williams, and P. Zoller, Quantum computations with atoms in optical lattices: Marker qubits and molecular interactions, *Phys. Rev. A* **70**, 012306 (2004).
 - [14] M. Anderlini, P. J. Lee, B. L. Brown, J. Sebby-Strabley, W. D. Phillips, and J. V. Porto, Controlled exchange interaction between pairs of neutral atoms in an optical lattice, *Nature* **448**, 452 (2007).
 - [15] S. Trotzky, P. Cheinet, S. Fölling, M. Feld, U. Schnorrberger, A. M. Rey, A. Polkovnikov, E. A. Demler, M. D. Lukin, and I. Bloch, Time-resolved observation and control of superexchange interactions with ultracold atoms in optical lattices, *Science* **319**, 295 (2008).
 - [16] B. Yang, H. Sun, C.-J. Huang, H.-Y. Wang, Y. Deng, H.-N. Dai, Z.-S. Yuan, and J.-W. Pan, Cooling and entangling ultracold atoms in optical lattices, *Science* **369**, 550 (2020).
 - [17] A. Impertro, S. Karch, J. F. Wienand, S. Huh, C. Schweizer, I. Bloch, and M. Aidelsburger, Local read-out and control of current and kinetic energy operators in optical lattices, *Phys. Rev. Lett.* **133**, 063401 (2024).

- [18] S. Zöllner, G. M. Bruun, and C. J. Pethick, Polarons and molecules in a two-dimensional Fermi gas, *Phys. Rev. A* **83**, 021603 (2011).
- [19] S. Murmann, A. Bergschneider, V. M. Klinkhamer, G. Zürn, T. Lompe, and S. Jochim, Two fermions in a double well: Exploring a fundamental building block of the Hubbard model, *Phys. Rev. Lett.* **114**, 080402 (2015).
- [20] T. Hartke, B. Oreg, N. Jia, and M. Zwierlein, Quantum register of fermion pairs, *Nature* **601**, 537 (2022).
- [21] Z. Zhu, Y. Kiefer, S. Jele, M. Gächter, G. Bisson, K. Viebahn, and T. Esslinger, Splitting and connecting singlets in atomic quantum circuits (2024), arXiv:2409.02984 [quant-ph].
- [22] M. Xu, L. H. Kendrick, A. Kale, Y. Gang, C. Feng, S. Zhang, A. W. Young, M. Lebrat, and M. Greiner, A neutral-atom Hubbard quantum simulator in the cryogenic regime, *Nature* **642**, 909–915 (2025).
- [23] C. Tabares, C. Kokail, P. Zoller, D. González-Cuadra, and A. González-Tudela, Programming optical-lattice Fermi-Hubbard quantum simulators, *PRX Quantum* **6**, 030356 (2025).
- [24] D. K. Mark, H.-Y. Hu, J. Kwan, C. Kokail, S. Choi, and S. F. Yelin, Efficiently measuring d -wave pairing and beyond in quantum gas microscopes, *Phys. Rev. Lett.* **135**, 123402 (2025).
- [25] D. González-Cuadra, D. Bluvstein, M. Kalinowski, R. Kaubuegger, N. Maskara, P. Naldesi, T. V. Zache, A. M. Kaufman, M. D. Lukin, H. Pichler, B. Vermersch, J. Ye, and P. Zoller, Fermionic quantum processing with programmable neutral atom arrays, *Proc. Natl. Acad. Sci.* **120**, e2304294120 (2023).
- [26] C. Sanner, L. Sonderhouse, R. B. Hutson, L. Yan, W. R. Milner, and J. Ye, Pauli blocking of atom-light scattering, *Science* **374**, 979 (2021).
- [27] S. H. Hauck and V. M. Stojanović, Coherent atom transport via enhanced shortcuts to adiabaticity: Double-well optical lattice, *Phys. Rev. Appl.* **18**, 014016 (2022).
- [28] C. Cicali, M. Calzavara, E. Cuestas, T. Calarco, R. Zeier, and F. Motzoi, Fast neutral-atom transport and transfer between optical tweezers, *Phys. Rev. Appl.* **24**, 024070 (2025).
- [29] T. Chalopin, P. Bojović, D. Bourgund, S. Wang, T. Franz, I. Bloch, and T. Hilker, Optical superlattice for engineering Hubbard couplings in quantum simulation, *Phys. Rev. Lett.* **134**, 053402 (2025).
- [30] P. Bojović, T. Hilker, S. Wang, J. Obermeyer, M. Barendregt, D. Tell, T. Chalopin, P. M. Preiss, I. Bloch, and T. Franz, High-fidelity collisional quantum gates with fermionic atoms (2025), arXiv:2506.14711 [quant-ph].
- [31] J. Nemirovsky and Y. Sagi, Fast universal two-qubit gate for neutral fermionic atoms in optical tweezers, *Phys. Rev. Res.* **3**, 013113 (2021).
- [32] J. Singh, J. A. Reuter, T. Calarco, F. Motzoi, and R. Zeier, Optimizing two-qubit gates for ultracold atoms using Fermi-Hubbard models, *Phys. Rev. Appl.* **24**, 034007 (2025).
- [33] F. Gkrtsis, D. Dux, J. Zhang, N. Jain, C. Gogolin, and P. M. Preiss, Simulating chemistry with fermionic optical superlattices, *PRX Quantum* **6**, 010318 (2025).
- [34] P. Bojović, Experimental data provided by the Max Planck Institute of Quantum Optics.
- [35] G. H. Wannier, The structure of electronic excitation levels in insulating crystals, *Phys. Rev.* **52**, 191 (1937).
- [36] W. Kohn, Analytic properties of Bloch waves and Wannier functions, *Phys. Rev.* **115**, 809 (1959).
- [37] W. Kohn, Construction of Wannier functions and applications to energy bands, *Phys. Rev. B* **7**, 4388 (1973).
- [38] Z. Hadzibabic and J. Dalibard, Two-dimensional Bose fluids: An atomic physics perspective, *Riv. Nuovo Cim.* **34**, 389 (2011).
- [39] E. Haller, M. J. Mark, R. Hart, J. G. Danzl, L. Reichsöllner, V. Melezhik, P. Schmelcher, and H.-C. Nägerl, Confinement-induced resonances in low-dimensional quantum systems, *Phys. Rev. Lett.* **104**, 153203 (2010).
- [40] F. Lorenzi, A. Bardin, and L. Salasnich, On-shell approximation for the s -wave scattering theory, *Phys. Rev. A* **107**, 033325 (2023).
- [41] T. Bergeman, M. G. Moore, and M. Olshanii, Atom-atom scattering under cylindrical harmonic confinement: Numerical and analytic studies of the confinement induced resonance, *Phys. Rev. Lett.* **91**, 163201 (2003).
- [42] D. S. Petrov and G. V. Shlyapnikov, Interatomic collisions in a tightly confined Bose gas, *Phys. Rev. A* **64**, 012706 (2001).
- [43] O. V. Sinkin, R. Holzlöhner, J. Zweck, and C. R. Menyuk, Optimization of the split-step Fourier method in modeling optical-fiber communications systems, *J. Light. Technol.* **21**, 61 (2003).
- [44] S. Montangero, E. Montangero, and Evenson, *Introduction to tensor network methods* (Springer, Cham, 2018).
- [45] W. Bao, S. Jin, and P. A. Markowich, On time-splitting spectral approximations for the schrödinger equation in the semiclassical regime, *J. Comp. Physics* **175**, 487 (2002).
- [46] R. L. Speth, W. H. Green, S. MacNamara, and G. Strang, Balanced splitting and rebalanced splitting, *SIAM J. Numer. Anal.* **51**, 3084 (2013).
- [47] B. Numerov, Note on the numerical integration of $d^2x/dt^2=f(x,t)$, *Astron. Nachr.* **230**, 359 (1927).
- [48] R. W. Hockney and J. W. Eastwood, *Computer simulation using particles* (CRC Press, Boca Raton, 2021).
- [49] I. Kuprov and C. T. Rodgers, Derivatives of spin dynamics simulations, *J. Chem. Phys.* **131**, 234108 (2009).
- [50] S. Machnes, E. Assémat, D. Tannor, and F. K. Wilhelm, Tunable, flexible, and efficient optimization of control pulses for practical qubits, *Phys. Rev. Lett.* **120**, 150401 (2018).
- [51] K.-T. Tang, *Mathematical Methods for Engineers and Scientists*, Vol. 3 (Springer, Berlin, 2007).
- [52] J. Singh, R. Zeier, T. Calarco, and F. Motzoi, Compensating for nonlinear distortions in controlled quantum systems, *Phys. Rev. Appl.* **19**, 064067 (2023).
- [53] F. Motzoi, J. M. Gambetta, S. T. Merkel, and F. K. Wilhelm, Optimal control methods for rapidly time-varying Hamiltonians, *Phys. Rev. A* **84**, 022307 (2011).
- [54] S. Yang, G. Masella, V. Moeini, A. Bellahsene, C. Li, T. Bienaimé, and S. Whitlock, Compact arbitrary optical waveform modulator with digital feedback, *Phys. Rev. Appl.* **23**, 054009 (2025).
- [55] P. K. Mogensen and A. N. Riseth, Optim: A mathematical optimization package for Julia, *J. Open Source Softw.* **3**, 615 (2018).
- [56] N. Khaneja, T. Reiss, C. Kehlet, T. Schulte-Herbrüggen, and S. J. Glaser, Optimal control of coupled spin dynamics: design of NMR pulse sequences by gradient ascent algorithms, *J. Magn. Reson.* **172**, 296 (2005).
- [57] P. de Fouquieres, S. Schirmer, S. Glaser, and I. Kuprov,

- Second order gradient ascent pulse engineering, J. Magn. Reson. **212**, 412 (2011).
- [58] M. Dalgaard, F. Motzoi, J. H. M. Jensen, and J. Sher-son, Hessian-based optimization of constrained quantum control, Phys. Rev. A **102**, 042612 (2020).